Inference of Cirrus Cloud Properties Using Satellite-observed Visible and Infrared Radiances. Part II: Verification of Theoretical Cirrus Radiative Properties

PATRICK MINNIS

Atmospheric Sciences Division, NASA Langley Research Center, Hampton, Virginia

PATRICK W. HECK AND DAVID F. YOUNG

Lockheed Engineering and Sciences Company, Hampton, Virginia

(Manuscript received 3 January 1992, in final form 20 July 1992)

ABSTRACT

A methodology is developed to apply a parameterization of radiative transfer calculations to satellite analyses of cirrus clouds. Cloud heights and optical depths are derived from visible and infrared window measurements taken during the First ISCCP (International Satellite Cloud Climatology Project) Regional Experiment (FIRE) when cirrus clouds were present. Geostationary satellite retrievals are compared to lidar-derived cloud heights and retrievals from a polar-orbiting satellite taken at different angles to determine which theoretical models of scattering phase function and single-scattering albedo best represent actual cirrus clouds. Models using small hexagonal ice crystals with a diameter of 20 μm (C20) and a size distribution of slightly larger hexagonal ice crystals representing a cirrostratus (CS) cloud produce the best results. The resulting mean cloud heights are within ± 0.3 km of the lidar results and have instantaneous uncertainties of ± 1.3 km. Mean cloud heights derived using a model based on water droplets with a 10-μm effective radius (ID) and a model based on a distribution of large ice crystals (cirrus uncinus, CU) are 1.3 km less than the lidar heights. The cloud height biases are due to overestimates of the cloud optical depths that are as much as 1.7 times greater than the C20 values. Reflectance patterns computed with the ice crystal models are consistent with the dual-satellite, multiangle observations of optical depth. Of the three ice-crystal models, the C20 model produced the least bias (3%), while the CU model yielded the greatest (12%). The ID-model optical depths derived using the geostationary satellite were 67% less than those from the polar-orbiting satellite. It is concluded that interpretation of cirrus reflectance with water-droplet models leads to biased results. This finding has important implications for the cirrus cloud properties derived by the ISCCP. The cloud-height and optical depth biases can be minimized with the use of the C20 or CS models.

1. Introduction

Visible (VIS; 0.65 μm) cloud optical depth can be used in satellite analyses to determine cloud infrared (IR; 11.5 μm) emittance and, subsequently, derive the equivalent blackbody temperature of the cloud using the observed IR radiance. In Part I of this paper, Minnis et al. (1993, hereafter referred to as MLT), developed a parameterization of VIS reflectance and IR emittance at the top of the atmosphere from radiative transfer calculations using various theoretical cloud particle-scattering phase functions and single-scattering albedos. This parameterization was then used to show that the optical depth for a given VIS reflectance observed by a satellite could vary substantially depending on the cloud microphysics. Thus, there is a potentially wide variation in the cloud temperatures and altitudes that could be inferred from a given VIS and IR radiance pair. In particular, MLT demonstrated that the inversion of VIS and IR radiances from a theoretical cirrostratus cloud using a model based on a water-droplet phase function, on average, overestimates a typical cirrus cloud temperature by ~ 15 K. This result translates to an underestimate of cloud height by 2 km or more for such optically thin clouds. Currently the International Satellite Cloud Climatology Project (ISCCP; see Schiffer and Rossow 1983) is using a model based on a water droplet distribution to derive VIS cloud optical depth and IR cloud emittance (Rossow et al. 1988). If real cirrus clouds have characteristics similar to those of the theoretical ice clouds examined by MLT, the cirrus optical depths and cloud heights derived by the ISCCP may be significantly biased. This paper attempts to verify if the theoretical models in the MLT study are representative of actual cirrus clouds.

Validations of theoretical phase functions have been attempted through both direct and indirect means. For example, Sassen and Liou (1979) used a cloud chamber, laser, and nephelometer to directly measure the

Corresponding author address: Dr. Patrick Minnis, Atmospheric Sciences Division, NASA, Langley Research Center, Mail Stop 420, Hampton, VA 23681-5225.

phase functions of small ice crystals (<20-μm mode radii) and compared them to Mie scattering calculations for spheres and cylinders. The theoretical and laboratory values showed poor agreement over most of the angular domain. Platt and Dilley (1984) determined values of the scattering phase function for a limited set of angles using lidar and solar radiometric data from cirrus clouds passing over a surface site. They found relatively good agreement with theoretical hexagonal ice-crystal values for the same range of scattering angles. Platt et al. (1980) correlated cirrus emittance and optical depths derived from a small satellite dataset to those expected from radiative transfer computations using two different phase functions. They found that the data agreed more closely with results of the calculations using a phase function for a cylinder rather than for a sphere. Takano and Liou (1989), in a more indirect approach, verified the maxima in their theoretical ice crystal phase functions by relating them to certain optical phenomena commonly observed below cirrus clouds. Wielicki et al. (1990) compared ratios of reflectances measured at two sets of angular pairs to radiative transfer calculations using various phase functions. Their results, though inconclusive, indicated that a phase function based on spherical particles produced the worst agreement with the data taken over cirrus clouds.

Two indirect methods are used here to determine which microphysical models best account for the VIS and IR radiances observed in scenes containing mostly cirrus clouds. The parameterization and models developed by MLT are applied to satellite-observed VIS and IR radiances to derive VIS cloud optical depths and cloud altitude. The cloud heights are then compared with lidar-derived cloud altitudes to evaluate the satellite-inferred values for four different cloud microphysical models. The uncertainties in the satellite-retrieved optical depths are estimated for various microphysical models by comparing the results from two different satellites viewing the same clouds from different angles. This study makes use of data taken during the initial First ISCCP Regional Experiment (FIRE) Intensive Field Observation (IFO) period (Starr 1987).

2. Data

Satellite data taken contemporaneously with collocated lidar measurements are first analyzed to estimate the cloud altitude errors resulting from the application of a given model to the analysis of a VIS-IR dataset. A set of dual-satellite data is then used to evaluate the bidirectional reflectance patterns generated using the theoretical phase functions in radiative transfer calculations as described by MLT. All the data were taken on days when cirrus was the predominant cloud type during the FIRE Cirrus IFO in October and November 1986 in the vicinity of Wisconsin. Since most of the data and analysis techniques have already been given by Minnis et al. (1990a, hereafter denoted as MHH) and Minnis et al. (1990b, hereafter denoted as MYSAG), only brief descriptions of them are given here. Additional data and methodology changes that were not included in those earlier studies are explained in more detail.

a. *Satellite radiances*

The primary radiance data consist of half-hourly 4 km $\times$ 8 km VIS and IR pixels from the Geostationary Operational Environmental Satellite (GOES-6). Two sets of data are analyzed. The first, used for comparison with surface or aircraft lidar measurements, is composed of strips of two-dimensional histograms of pixel pairs corresponding to the distance traveled in one-half hour by a cloud over the surface site or by the aircraft over a cloud field (see MYSAG). Figure 1 shows an example of the GOES VIS and IR imagery for 19 October 1986 centered near the western border of Minnesota. The ER-2 aircraft flight track, superimposed on the imagery, traverses a field of high cirrus clouds.

The second dataset was constructed from two-dimensional histograms of VIS and IR pixel pairs located in 0.5° regions within a 5° $\times$ 5° area, designated the IFO grid, centered over Wisconsin (see MHH). The two-dimensional histograms were compressed as described by MHH. A supplementary dataset was used to obtain clear-sky reflectances and temperatures for ER-2 flight tracks outside of the IFO grid. This dataset consists of VIS-IR histograms for 2.5° $\times$ 2.5° regions.

The GOES VIS data, stored as counts, D (where $0 < D \leq 63$), in the histograms are converted to radiance and VIS reflectance,

$$\rho_G = (0.1624 D_G^2 - 8.3)/(525.9\mu_0), \qquad (1)$$

where μ_0 is the cosine of the solar zenith angle, θ_0. The raw GOES IR data are given as equivalent blackbody temperatures, T, and converted to radiance with the Planck function evaluated at 11.5 μm.

Two-dimensional, VIS-IR histograms were also derived from the NOAA-9 Advanced Very High Resolution Radiometer (AVHRR) Global Area Coverage (GAC) 4-km data on the 5° grid to coincide with the GOES data. The NOAA-9 daytime pass over Wisconsin occurred between 1930 and 2100 UTC ($\sim$1430 local time). The AVHRR channel-1 VIS reflectance is

$$\rho_A = (0.6060 D_A - 22)/(519.4\mu_0), \qquad (2)$$

where D_A is the AVHRR 10-bit count. The VIS calibrations for both GOES and AVHRR were provided by Charles H. Whitlock (personal communication, 1989). GOES-equivalent IR temperatures were computed for the AVHRR by averaging the equivalent blackbody temperatures for channels 4 (10.8 μm) and 5 (11.7 μm).

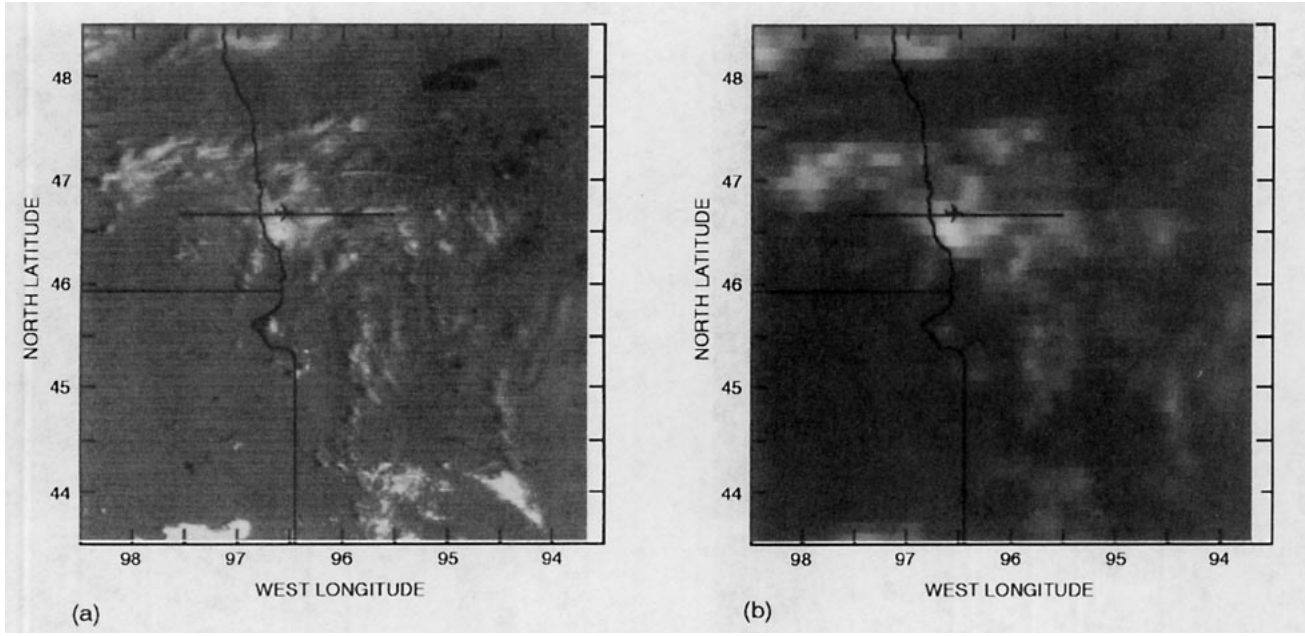

FIG. 1. GOES images and ER-2 flight tracks from 1630 UTC 19 October 1986: (a) VIS and (b) IR.

Values for θ_0 and the viewing zenith and relative azimuth angles, θ and ψ, respectively, were computed for each set of measurements. During the IFO, GOES-6 was located over the equator at approximately 97°W. This location yields a value of $\theta \sim 52°$ for Wisconsin. The GOES relative azimuth angles were mainly confined to the backward-scattering directions. The orbital precession of the *NOAA-9* produces a variation in θ between 0° and 70° over a given site every 4–5 days. Because of its cross-track scan pattern, the AVHRR views a given site from relative azimuth angles that lie in both the forward and backward hemispheres at a nearly constant skew to the solar plane. The skew depends on both the solar and site latitudes.

Consequently, a range of solar zenith angles with relatively constant viewing angles is covered using the GOES, while a range of viewing angles at a nearly constant θ_0 is covered with the AVHRR. Table 1 summarizes the angular conditions for the GOES and matched AVHRR data. It includes values for the scattering angle, Θ, corresponding to each set of viewing and illumination conditions. All values are approximate since the angles vary by up to 10° over the Wisconsin region at a given time. Although the GOES and AVHRR angles are nearly the same for 28 October, the satellite azimuths are different. GOES is on one side of the solar plane; *NOAA-9* is on the other, resulting in different viewing conditions. The GOES solar zenith and scattering angles, respectively, vary from 80° and 109° at 1330 UTC to 56° and 175° at 1830 UTC back to 81° and 125° at 2200 UTC. Angles for the GOES at other times are given by MYSAG. The only view in the forward-scattering hemisphere is for the AVHRR during 27 October.

Figure 2 shows an example of these matched satellite images over Wisconsin for 2 November 1986. The AVHRR is viewing the scene from a near-nadir angle (Table 1). Differences in the viewing angles are evident in the upper right quadrant of the IR images. Visibly thin cirrus clouds in this area show relatively little gradation in GOES IR brightness compared to the AVHRR clouds. The GOES viewing angle diminishes the transmittance of the marginally thin clouds so that they appear as cold (white) as the thick clouds in the center of the large cloud masses. Other examples of the matched images are found in MHH.

b. *Lidar measurements*

Lidar backscatter data can be used to define the cloud base and thickness. Under conditions of small attenuation and constant backscatter phase function, the backscatter intensity profiles indicate the vertical distribution of cloud extinction. During the FIRE Cirrus IFO, four ground-based lidars acquired nearly continuous lidar backscatter profiles during periods with well-

TABLE 1. Approximate angles of matched GOES and AVHRR data in degrees.

		GOES angles				AVHRR angles		
Day	Time (UTC)	θ	Ψ	Θ	θ_0	θ	Ψ	Θ
22 Oct	2035	53	148	142	69	9	145	118
27 Oct	1935	53	161	162	61	53	40	76
28 Oct	2100	53	140	140	73	49	147	143
30 Oct	2040	53	142	145	70	28	143	127
2 Nov	2000	53	155	154	68	18	38	96

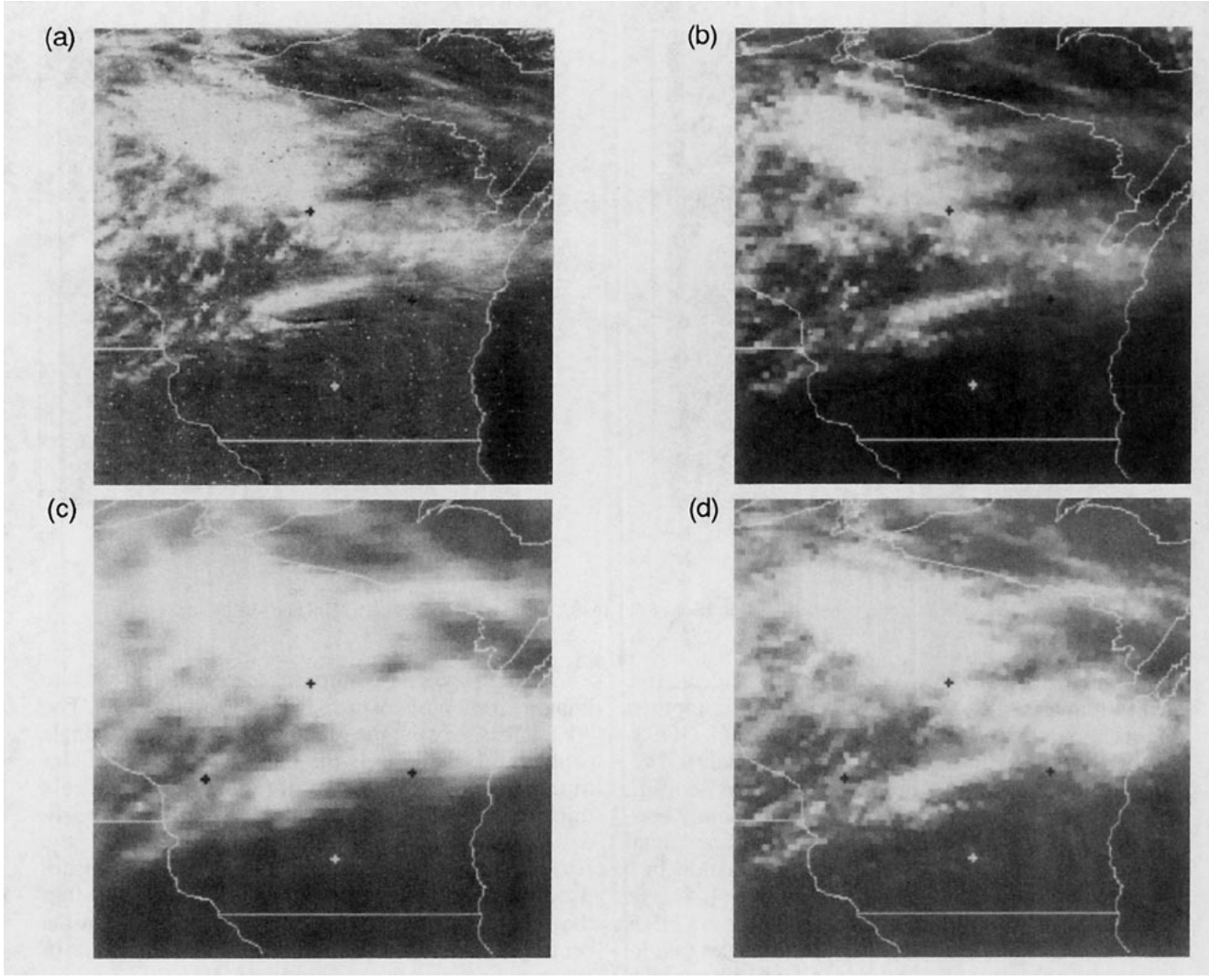

FIG. 2. Satellite imagery from 2006 UTC 2 November 1986: (a) GOES VIS, (b) AVHRR VIS, (c) GOES IR, and (d) AVHRR IR.

defined cirrus systems (Sassen et al. 1990). Data taken from three of these lidars are used in this study. The University of Utah mobile polarization lidar was located at Wausau, Wisconsin. The NASA Langley ground lidar was situated at Ft. McCoy, Wisconsin, while the University of Wisconsin high spectral-resolution lidar was in Madison. Ground-based lidars provide excellent definition of cloud base. If the clouds are optically thin, the lidar beam can penetrate through the cloud and reveal some of the cloud's vertical structure and the altitude of its top. The maximum penetration depth depends on the lidar's wavelength and power.

The high-altitude ER-2 aircraft was equipped with a down-looking lidar that was used to define cloud structure over various locations in the vicinity of Wisconsin during the IFO. Data from the IFO ER-2 flights are summarized by Spinhirne et al. (1988). The ER-2 lidar outlines the cloud top. Depending on the cloud thickness, this airborne lidar can also penetrate through the cloud and determine its base altitude. The ER-2 data included in this study are summarized in Table 2. These data were taken over Wisconsin, Minnesota, and Iowa at various times during the IFO.

TABLE 2. Summary of ER-2 cloud lidar data.

Day (October 1986)	Times (UTC)	Height range (km)
13	2000–2030	8.0–8.5
19	1630–1830	9.1–10.3
21	1800–1830	11.4–11.7
22	1500–1730	9.3–10.3
24	1830–2100	9.5–9.6
27	1830–2100	8.0–8.5
28	1600–1800	9.3–10.0
31	1730	12.5

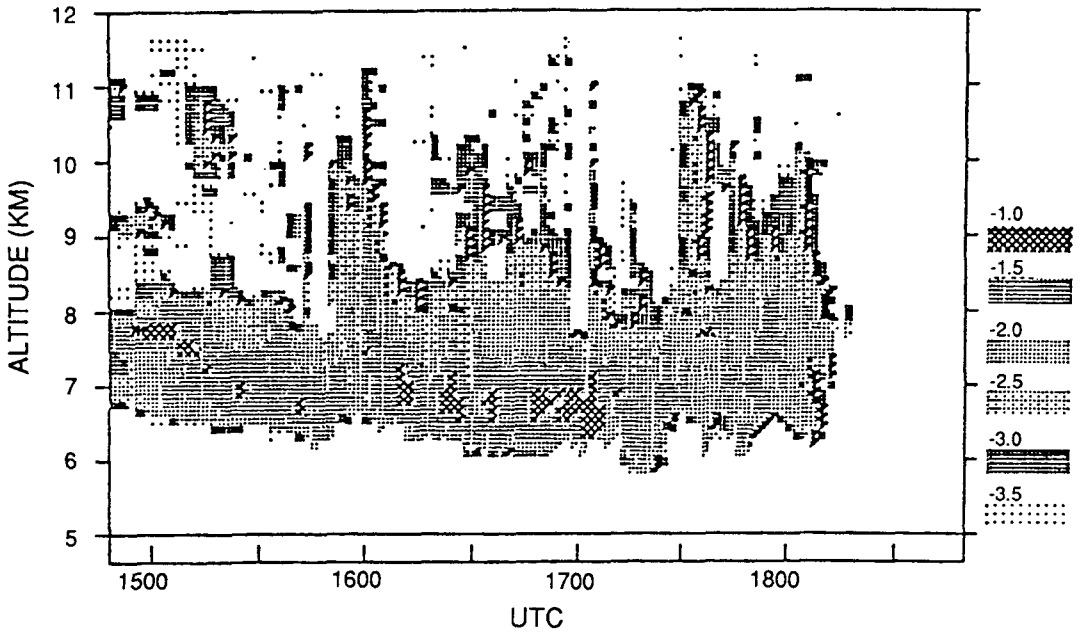

FIG. 3. Estimated lidar volume extinction efficiencies from cirrus clouds over Wausau on 28 October 1986. Adapted from Minnis et al. (1990b).

An example of ground-based lidar returns shown in Fig. 3 (adapted from MYSAG) defines the outlines of the cirrus clouds as they passed over Wausau during the morning of 28 October 1986. The shading represents various amounts of cloud extinction. Cloud base, z_b, drops from ~6.8 km at 1500 to ~5.8 km at 1720 UTC. Cloud-top altitude, z_t, varies between 11.5 km and ~8 km. The particle backscattering efficiency depends on cloud-particle shape and phase. Additional information concerning the lidar returns is found in Sassen et al. (1990). All of the ground-based lidar cases described by MYSAG are used here.

Four parameters were derived from plots like that in Fig. 3 by graphically averaging the data within ±15 min of the UTC half hour plus 5 minutes to match the times of satellite observation. The cloud thickness is $h = z_t - z_b$. Mean cloud center height, z_c, is taken as a simple average of z_t and z_b in most cases. MYSAG attempted to define the cloud center as the backscatter-intensity-weighted center to account for the variable distribution of mass in the cloud. Except for Madison, their definition required the assumption that the cloud top was always observed. The same method is used here only for those ER-2 data having a continuous ground return during the pass. For the remainder of the ER-2 data and the surface sites, the simpler averaging method is used to avoid the uncertainty of the cloud structure below (ER-2) or above (surface) initial cloud scattering altitude. Lidar returns from ER-2 overflights are also more carefully employed here to better define the cloud-top altitude over the surface sites whenever possible. The cloud-center height is adjusted as in MYSAG whenever its corresponding temperature is warmer than the coldest satellite-observed temperature.

Since the clouds are advecting over the fixed surface sites, the averaged lidar data correspond to a thin vertical cross section taken out of some cloud volume. It is assumed that the cross-section-averaged data represent the mean conditions of that volume. MYSAG estimated that the uncertainty in z_c derived with the graphical method from ground-based lidar was ±0.7 km assuming that the cloud top was known. Similar errors are expected for the airborne lidar assuming cloud-base altitude is known. The uncertainty is primarily due to the vertical variation of the cloud over a half-hour time period or its equivalent distance. If the clouds are thick (e.g., $\tau > 4$), the cloud-base or cloud-top altitude is usually indeterminate. An additional cloud height uncertainty of ±0.4 km is incurred in the ER-2 data because of variations in flight altitude that were not taken into account in the initial lidar data analysis (Spinhirne et al. 1988).

An example of the ER-2 lidar traces is shown in Fig. 4. This plot was redrawn from a rough figure presented by Spinhirne et al. (1988). The data correspond to approximately 200 km of the flight track drawn in Fig. 4a. The vertical cloud structure is very complex. The clouds are relatively continuous between 7 and 10 km. Part of the main cloud field is overlaid with a thin layer at ~11 km. Cloud center height for this cloud field was estimated to be 9.0 km. The surface backscatter is seen whenever the cloud is sufficiently thin. Flight tracks containing significant contamination from lower-level ($z < 6$ km) clouds were eliminated from the study.

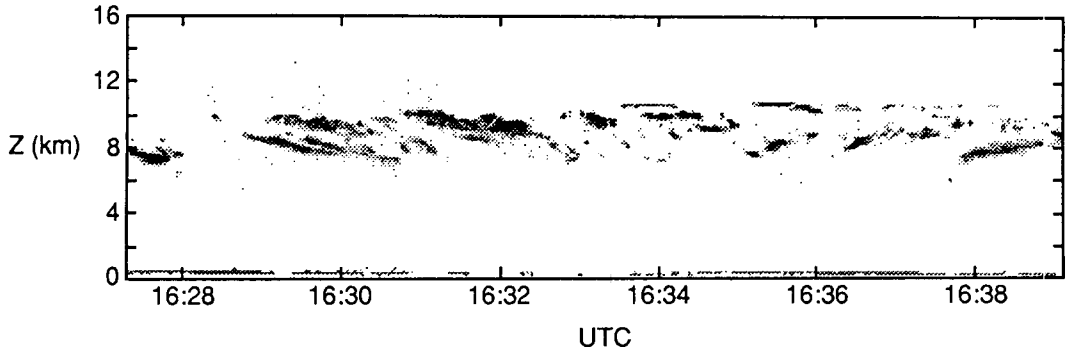

FIG. 4. ER-2 lidar profile of clouds corresponding to flight track in Fig. 1. Redrawn from Spinhirne et al. (1988).

c. Temperature and pressure data

Soundings from Green Bay, Wisconsin, are used to determine temperature–height relationships for most of the lidar data. Mean cloud-top, cloud-base, and cloud-center temperatures, T_t, T_b, and T_c, respectively, correspond to z_t, z_b, and z_c on the soundings. Soundings taken from the ISCCP C1 data tapes (Rossow et al. 1988) are used to estimate these same temperatures for the ER-2 flights before 22 October 1986. The C1 temperature data are available for nine selected pressure levels only. Surface temperatures taken every 6 hours at Madison, Wausau, and Lone Rock, Wisconsin, and occasionally at Ft. McCoy, are used to supplement the clear-sky temperatures derived from the satellite data. A surface pressure of 990 mb was assumed for all of the analyses.

3. Analysis methodology

Cloud-center and cloud-top altitude and cloud optical depth are determined from the satellite data using the VIS-IR parameterization detailed in MLT and briefly summarized in the following subsection. Values for clear-sky temperature and reflectance are needed to solve the model equations. Certain constraints and averaging processes are also required to arrive at reasonable solutions in some cases. These components of the analysis system are also described in this section.

a. Parameterization

For a cloudy scene, the VIS reflectance is modeled as

$$\rho = (\rho_1 + \rho_2 + \rho_3 + \rho_4 + \rho_5)/(1 - \zeta), \quad (3)$$

where ρ_1 accounts for the cloud reflectance and Rayleigh scattering above the cloud. It is attenuated by ozone absorption above the cloud. The cloud reflectance is

$$\rho_c = \rho_c(k, \tau; \theta_0, \theta, \psi),$$

where τ is the cloud optical depth and k is the cloud microphysical model. The second term, ρ_2, is the direct reflectance from the surface and atmosphere that has not been attenuated by the cloud; it depends on the clear-sky reflectance, ρ_s, cloud optical depth, and the forward-scattering properties of the cloud microphysical model. The third term, ρ_3, accounts for the first-order diffuse reflectance from the surface that passes back through the cloud. It depends on the cloud albedo $\alpha_c(k, \tau; \theta_0)$, the diffuse cloud albedo $\alpha_{cd}(k, \tau)$, and the diffuse clear-sky albedo α_{sd}. The fourth term, ρ_4, accounts for diffuse radiation from the surface and below-cloud atmosphere that undergoes successive scatterings with the cloud. It also depends on α_c and α_{cd} and accounts for the altitude of the cloud. The fifth term, ρ_5, is based on a regression fit to account for additional reflectance from the surface that was not included in the other terms. It impacts the reflectance only in thin-cloud cases and depends on τ, μ_0, ρ_s, and α_{sd}. The regression coefficients depend on the microphysical model. The term in the denominator, ζ, is a regression-fit correction factor to account for small deviations of the parameterization from the radiative transfer calculations. Its value depends only on the microphysical model.

The cloud effective emittance is

$$\epsilon = 1 - \exp[a(\tau/\mu)^b], \quad (4)$$

where μ is $\cos\theta$, and a and b depend on the microphysical model. For a cloudy pixel, the radiance corresponding to the observed temperature T is

$$B(T) = \epsilon B(T_c) + (1 - \epsilon)B(T_s), \quad (5)$$

where B is the Planck function at 11.5 μm and T_s is the clear-sky temperature. Additional details and exact formulations of the reflectance and emittance parameterizations are given by MLT.

In this study, lookup tables of ρ_c, α_c, and α_{cd} computed for four sets of cloud microphysical optical properties are used to interpret the satellite data. The microphysical characteristics represented in the lookup tables are as follows. The ID model, based on a water-droplet distribution having an effective radius of 10 μm, is used to represent the ISCCP cloud radiative transfer model. The C20 model, based on the optical

properties of a randomly oriented hexagonal ice crystal having a length-to-diameter ratio, $L/2a$, equal to 20 μm/20 μm, is used to represent small ice crystals. The CS model based on a size distribution of randomly oriented hexagonal ice crystals represents a cirrostratus cloud (equivalent $L/2a \approx 85$ μm/40 μm). The CU model, based on large, randomly oriented hexagonal ice crystals, is representative of a cirrus uncinus cloud (equivalent $L/2a \approx 400$ μm/120 μm). The three ice-crystal models account for the range of particle sizes typically found in cirrus clouds. The optical properties of these clouds at the VIS and IR wavelengths and the development of the lookup tables are given by MLT. The coefficients for the terms in (3) and (4) are also found in MLT.

b. *Clear-sky temperature and reflectance*

The clear-sky temperatures for the strip data are estimated from the satellite data by following the approach outlined by MYSAG. Clear-sky temperatures for the gridded data are found using the techniques of Minnis et al. (1987). When no clear pixels are available near the site, corrected surface observations of air temperature are used to estimate clear-sky temperature.

Over Wisconsin, values of clear-sky reflectance are computed for each region using the 0.01° clear-sky albedo map of the IFO area constructed by MHH from minimum reflectance data at each hour. Clear-sky reflectance over any latitude, λ, and longitude, ϕ, of the grid at time, t, is estimated as

$$\rho_s(\lambda, \phi, t, \theta_0, \theta, \psi) = \alpha_s(\lambda, \phi, t, \theta_0)\chi_s(\theta_0, \theta, \psi),$$

where χ_s is the clear-sky anisotropic reflectance factor with values given by the model of Minnis and Harrison (1984) for water and land and α_s is the clear-sky albedo. Since the full range of solar zenith angles is not observable at the latitude of Wisconsin during October, the clear-sky diffuse albedo is taken to be the noontime value that corresponds to $\theta_0 \approx 56°$. Mean hourly clear-sky reflectances were also determined for a 2.5° latitude–longitude grid that encompasses the area between 30° and 50°N and between 60°W and 125°W. Clear-sky reflectances for the ER-2 flight tracks outside of the IFO grid were assumed to be the same as the clear-sky reflectance for the 2.5° region containing the flight tracks.

c. *Histogram analysis method*

The analysis of the two-dimensional histograms basically follows the procedures of MHH. These procedures and notable changes are briefly reviewed here.

Given the relationships between cloud reflectance and emittance, it is possible to define the variation of D and T for a cloud having the radiative-center temperature, T_c. This variation, defined by a set of count–temperature pairs for discrete data, follows from (5) and is given by the function,

$$T_\epsilon = T_\epsilon(D, T_c) = B^{-1}\{\epsilon(D)B(T_c) + [1 - \epsilon(D)]B(T_s)\}. \quad (6)$$

The emittance $\epsilon(D)$ is found using (1) or (2), (4), (5), and the appropriate values for the input variables. Thus, a temperature corresponding to a cloud having T_c may be defined for any given count (reflectance) and microphysical model.

Figure 5 shows a schematic drawing of a VIS-IR histogram given in IR temperature and GOES VIS counts. The histogram is divided into five areas: clear, low cloud, middle cloud, high cloud, and dark pixel or stratospheric cloud. The clear area incorporates all pixels having $T > T_s - \Delta T$ and $D \leq D_t$, where ΔT is the cloud threshold difference. Its value is 6 K over land and 3 K over water in this study. The clear-sky VIS threshold count is D_t as defined by Minnis et al. (1987). All other pixels are assumed to be overcast. Low-cloud pixels are all those having the count D where $D > D_t$ and $T > T_\epsilon(D, T_m)$. The temperature T_m is the temperature from the sounding corresponding to $z = 2$ km. Similarly, the high-cloud pixels are those having the count D and temperature $T \leq T_\epsilon(D, T_h)$, where T_h is taken from the sounding for $z = 6$ km. All nonclear pixels with temperatures and counts between the low- and high-cloud pixels are middle-cloud pixels. An upper boundary, $T_\epsilon(D, T_p)$, is computed to correspond to the tropopause temperature, T_p, minus 2 K. The 2 K subtraction accounts for uncertainty in the soundings. The curves corresponding to these cloud boundaries are shown in Fig. 5 and are labeled as P_m, P_h, and P_p. The pixels that are darker and colder than the counts and temperatures defining P_p are designated dark or stratospheric cloud pixels. These pixels, discussed extensively by Minnis et al. (1990b), are treated in a special manner as described below.

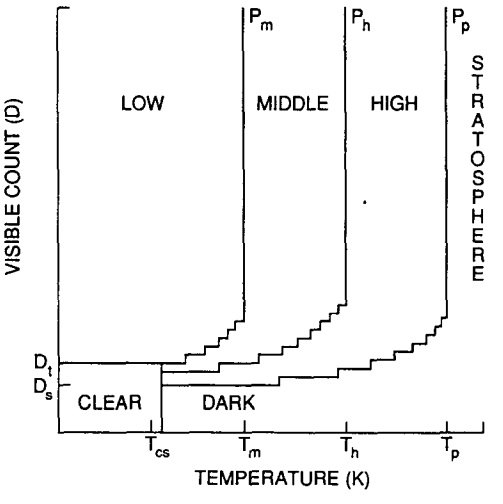

FIG. 5. Schematic VIS–IR histogram illustrating boundaries for clear-sky and cloud-layer classifications.

In this analysis there are four layers, $k = 1, 2, 3$, and 4, or clear, low, middle, and high, respectively. The areal fraction of a scene assigned to a given layer is

$$C_k = N_k/N_t,$$

where

$$N_k = \sum_{ij} n(T_i, D_j),$$

n is the number of pixels having T_i and D_j, the limits i and j are defined only for layer k, and N_t is the total number of pixels in the histogram. The temperatures in a given layer are averaged for each VIS count. Thus, for D_j,

$$T_{kj} = B^{-1}[\sum_i B(T_i)n(T_i, D_j)/N_{kj}],$$

where

$$N_{kj} = \sum_i n(T_i, D_j).$$

The emittance, $\epsilon_j = \epsilon(D_j)$, for each VIS count is used to adjust T_{kj} using (6) to solve for $T_c(kj)$. The pressure in the middle of the layer is used to compute Rayleigh scattering for all clouds in the layer.

If D_j is in the dark pixel area of the histogram, ϵ_j is indeterminate. It is assumed that dark pixels result from shadowing effects, other finite cloud effects, and inadequacies in the microphysical scattering models. When dark pixels are encountered, high-cloud pixels having greater brightness values are included in the summation to raise the mean, combined reflectance to a value of $D > D_s$ so that ϵ can be computed. If there are no low- or middle-cloud pixels having $\tau > 1$, then high- or middle-layer pixels having the same temperature as the dark pixels are included in the summation. The summation continues with the next brightest visible count until the mean count is greater than D_s. Pixels having temperatures lower than the coldest dim pixels are included in the summation only if the mean value of D remains in the dark-pixel area of the histogram. If the summation process does not result in a nondark mean value of D, it is assumed that the dark pixels are clear, but shadowed. Although dark pixels comprised only 3% of pixels in the cirrus cases of Minnis et al. (1990b), they can account for a much larger percentage of the pixels in a given scene and must be considered in any analysis scheme.

If the initial value of $T_c(kj)$ for any kj is less than T_p, then the summation process used for the dark pixels is invoked until $T_c(kj) \geq T_p$. If this condition is never satisfied for the data, then it is assumed that the cloud is located at the tropopause. The mean emittance and optical depths are then adjusted to force this solution. Finally, the average temperature for layer k is

$$T_k = B^{-1}\{[\sum_j N_{kj}B(T_c(kj))/N_k]\},$$

where T_j is the mean temperature for each VIS count, D_j. In the exceptions noted above, the index and values of D_j are adjusted to reflect the change in summation. No pixel values are ever used twice.

Mean optical depths for each layer are found in a similar manner:

$$\tau_k = \sum_j \tau(D_{kj})n(D_{kj})/N_{kj}.$$

Again, the indices and values of D_{kj} are adjusted for the dark- or tropopause-adjusted pixels discussed above.

The total cloud fraction is

$$C = C_2 + C_3 + C_4,$$

and the mean cloud-center temperature is

$$T_c = B^{-1}\{[\sum_{k=2}^{4} C_kB(T_c(k))/C]\}.$$

Cloud-top temperature for each layer is also estimated using the empirical model of MHH, the mean layer emittance, and layer cloud-center temperature. Mean layer emittance is found from (6), where the adjusted cloud-center temperature is T_c and the radiative-mean, unadjusted layer temperature is T_ϵ.

These parameters are computed for the strip data using each microphysical model and compared to the lidar results. The cloud heights derived from the strip data are used to evaluate the accuracy of the cloud heights determined with the analysis method. The parameters are also computed for the gridded data from both the GOES and AVHRR for intercomparison. The optical depths derived from the gridded data are intercompared to evaluate the theoretical scattering patterns from the model lookup tables.

4. Results

a. Cloud-height comparisons

The satellite-derived cloud-center heights are compared with all 83 surface lidar results in Fig. 6. Mean cloud height differences Δz_c and their standard deviations are also shown. Both the ID (Fig. 6a) and CU (Fig. 6d) models tend to underestimate the lidar cloud heights by an average of 1 km. Very few of the ID and CU cloud heights are greater than the surface-derived values. The C20 model overestimates the cirrus altitudes by 0.4 km, while the CS results match the lidar heights the best on average. The scatter in the data is virtually the same for all four models, indicating that much of it arises from other factors. These other error sources are discussed later.

Mean cloud-center altitude from the surface-lidar data is 9.1 km. The average surface-cloud temperature difference is roughly 40 K. The mean optical depths are 4.0, 2.2, 2.5, and 3.4 for the ID, C20, CS, and CU models, respectively. From Fig. 25 in MLT, a difference

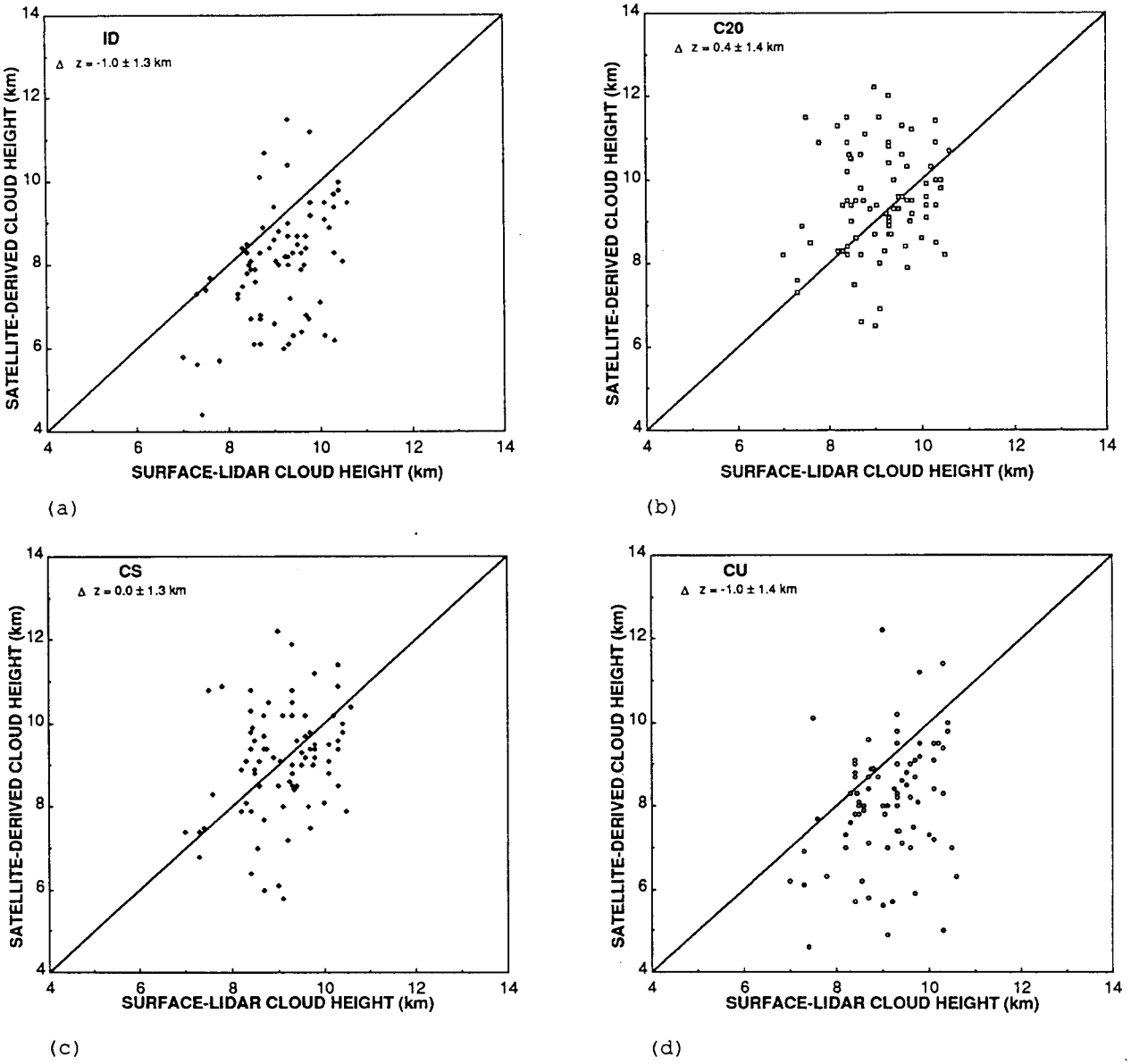

FIG. 6. Comparison of GOES and surface-lidar cloud heights using (a) ID model, (b) C20 model, (c) CS model, and (d) CU model.

of ~6 K in T_c or ~1 km in z_c between the CS and ID models is expected for these conditions. The results in Fig. 6 are consistent with this expectation indicating that the parameterization is being properly applied to the data.

Figure 7 shows the mean height differences for three of the models as functions of UTC. The greatest errors for all of the models occur at 1330 UTC when $\theta_0 \approx 81°$ and $\Theta = 109°$. The latter angle corresponds to the minimum in the water-droplet phase function (MLT) used for the ID model and a relative maximum in the CS phase function. The mean lidar heights are midway between the ID and ice-crystal results. Of the four cases constituting the 1330 UTC averages, two are from 28 October when cirrus was overlying an altocumulus deck containing water droplets (Sassen et al. 1990). The average CS overestimate on that day was 2.2 km. The other two heights were taken during 22 October when the mean CS heights were only 1 km greater than the lidar values. No evidence of droplets was reported in the lidar logs during 22 October. During all of the other UTC hours, the mean CS heights are within ±1 km of the surface-lidar cloud altitudes.

The only times when the mean ID heights are greater than the CS values are around 1500 and 2100 UTC when $\Theta \approx 135°$ (see MYSAG). This angle corresponds to the superposition of a relative scattering maximum in the ID phase function on the minimum in the ice-

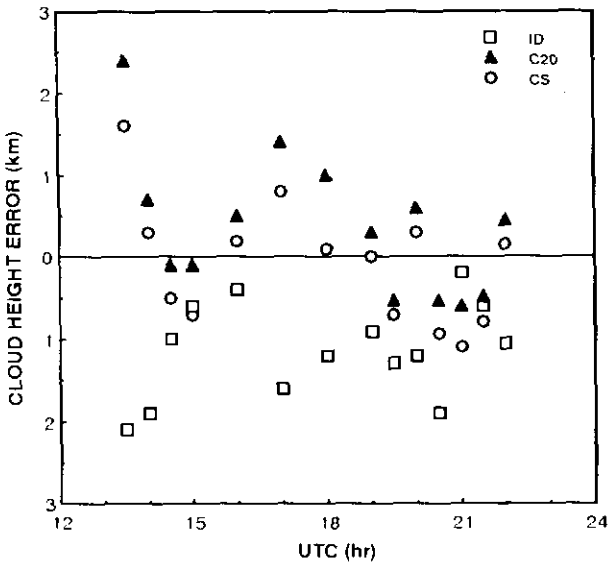

FIG. 7. Mean cloud height error over surface-lidar sites for three models as a function of time (UTC) for 22 October–2 November 1986.

crystal phase function (MLT). This results in an ID optical depth slightly smaller than the CS optical depth for the same reflectance. Thus, somewhat greater cloud heights are derived with the ID model.

The trends seen in the surface–satellite comparisons are also evident in the aircraft–satellite results shown in Fig. 8. In these data, the mean satellite-derived cloud heights are lower than those from the surface-satellite comparison relative to the lidar values. This is especially true for the ID and CU models. The reason for the lower heights may be related to the analysis of the lidar data or to differences in the sampled clouds. In the former case, there may be a tendency to obtain higher cloud tops with the down-looking lidar because the uppermost clouds are so well defined. The mean ER-2 lidar cloud height is 9.5 km, slightly greater than that for the surface cases. This greater height corresponds to a larger surface–cloud thermal contrast, which tends to increase the relative bias between the CS and ID results (MLT). These data were also averaged according to UTC. Again, the only hours when the ID values were greater than the CS heights were near 1500 and 2100 UTC.

The ER-2 and surface results were combined and are summarized in Table 3, where σ denotes standard deviation. The total number of samples is 109 and the mean cloud height is 9.2 km. The CU and ID models both underestimate cloud height by 1.3 km, while the C20 and CS models produce cloud heights that are nearly unbiased on average. The cloud height uncertainties associated with the latter models are also smaller than the former values. The ID model produces significantly greater (~64% higher) optical depths than either the CS or C20 models, as expected from theoretical calculations (MLT).

The histogram analysis approach used here is slightly different from the algorithm employed by the ISCCP. Each pixel pair is interpreted with the radiative transfer model individually in the ISCCP method. Thus, there is no averaging of dark pixels with brighter pixels or of "stratospheric" pixels with warmer pixels to attempt a valid solution of the cloud height retrieval. Pixels that do not produce a tropospheric solution ($T_c > T_p - 5$ K) in the ISCCP method are set to the lowest temperature limit and a cloud height is computed. The resulting cloud heights are then averaged to find a mean cloud height for the region. To determine if this averaging approach makes any difference, the surface-lidar cases were reanalyzed using the ISCCP algorithm with the ID model. The resulting ISCCP cloud heights are 0.3 km lower than the ID results in Fig. 6a. Thus, it is expected that the application of the actual ISCCP algorithm to this dataset would yield mean cloud heights at least 1.5 km lower than the lidar values.

b. AVHRR-GOES comparisons

The lidar comparisons provide a validation of one aspect of the cloud properties, namely cloud height. A correct cloud height suggests that the derived optical depth is also correct. Another feature of the cirrus properties that is important for remote sensing or simulation is the radiance field produced by the cloud. A correct retrieval of cloud optical depth implies that the radiance field is being adequately simulated with a model. In the previous section, the CS and C20 models produced reasonable estimates of cloud height and, therefore, cloud optical depth for solar zenith angles between 55° and 82°. The viewing zenith angle, however, was restricted to 51°–53°, a small portion of the

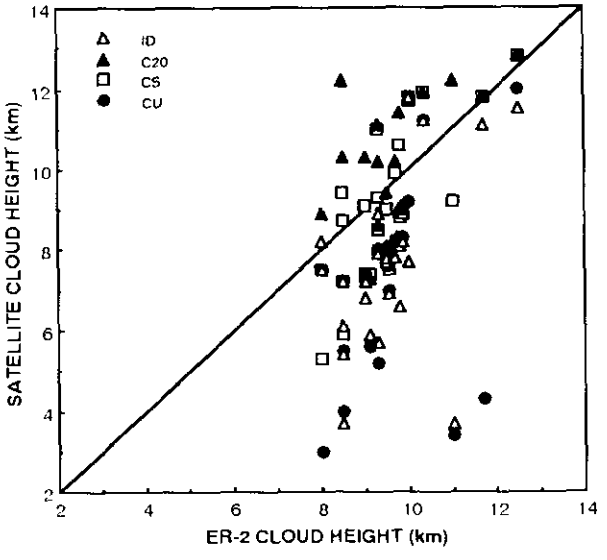

FIG. 8. Comparison of ER-2 and GOES-derived cloud heights for 13–31 October 1986.

TABLE 3. Summary of cloud properties from GOES-lidar comparisons.

Model	Δz_c (km)	$\sigma(\Delta z_c)$ (km)	τ
ID	−1.3	1.7	4.1
C20	0.3	1.4	2.4
CS	−0.1	1.3	2.6
CU	−1.3	1.8	3.6

possible range. To better ensure that the lidar–satellite comparisons are not simply fortuitous, it is necessary to attempt retrievals from other angles. If the radiance field is properly simulated, the optical depths and heights measured from one set of angles should be the same as those from other angles. This section presents comparisons of the results derived from the matched AVHRR and GOES 0.5° regional data. Only those data from regions that are at least 90% land or water and have $C > 20\%$ for both satellite retrievals are included in the comparisons.

Figure 9 shows the comparisons of the AVHRR- and GOES-derived cloud heights for the four microphysical models. Using the GOES CS results as a guide, it is evident that the clouds are mostly above 6 km. The mean GOES cloud altitudes are 7.5, 9.3, 9.0, and 8.0 for the ID, C20, CS, and CU models, respectively. Except for the lowest clouds, the GOES ID cloud

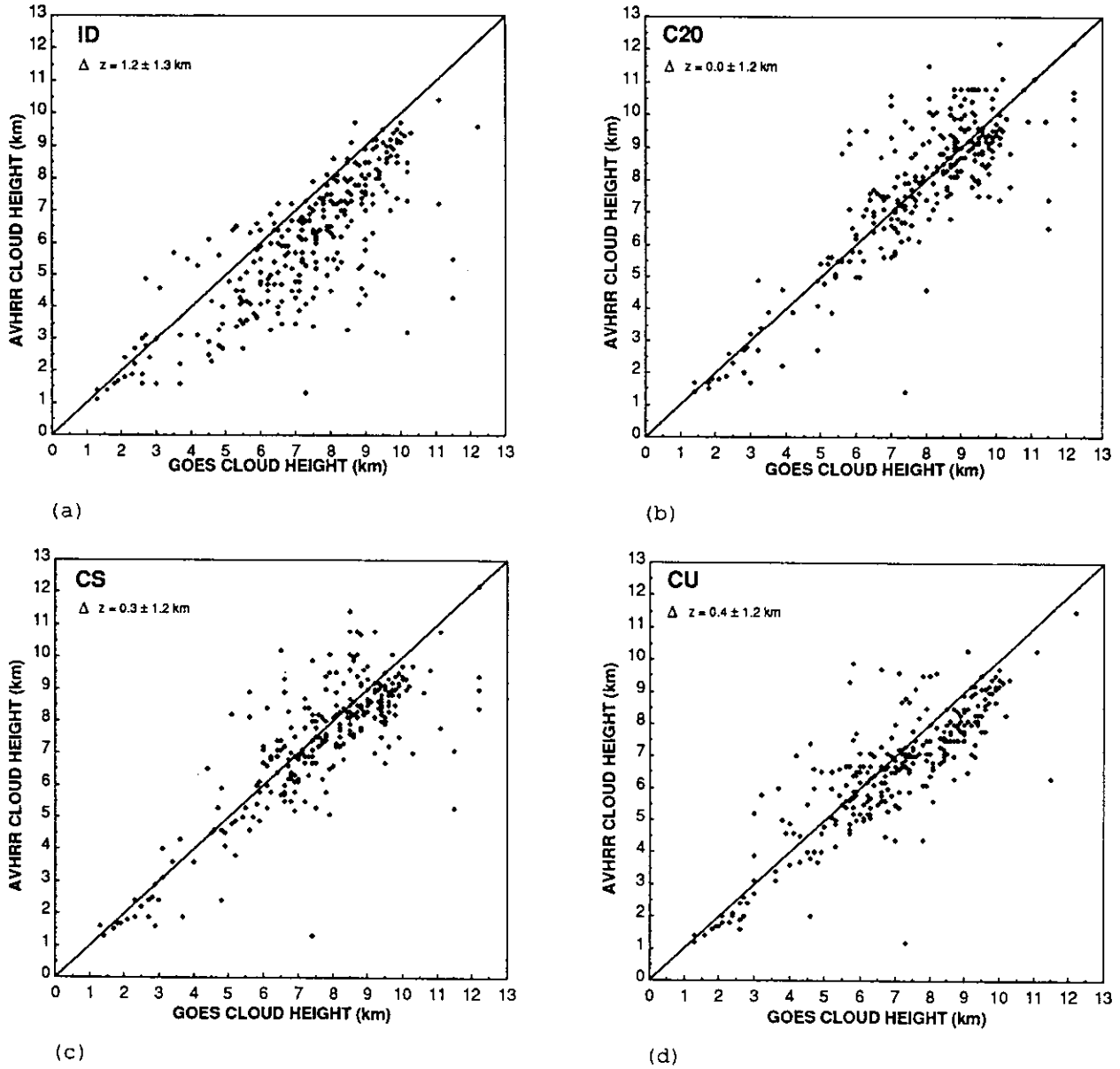

FIG. 9. Comparison of cloud heights from AVHRR and GOES for (a) ID model, (b) C20 model, (c) CS model, and (d) CU model.

heights are generally above the corresponding AVHRR values (Fig. 9a). Overall, for the 286 cases, the AVHRR ID clouds are 1.2 km lower than their GOES counterparts. All three ice-crystal models produce much better cloud height correspondence between the two satellite analyses. The C20 heights are the least biased, while the AVHRR CU cloud altitudes are 0.4 km lower than the GOES values. The scatter in the height comparisons is nearly the same for all of the models. It is either less than or equal to the variance seen in the lidar comparisons.

Optical depths derived from the two satellite datasets are compared in Fig. 10 for all four models. Means and standard deviations of $\Delta\tau = \tau(\text{AVHRR}) - \tau(\text{GOES})$ are also shown in Fig. 10. The scale in these figures was chosen to highlight the comparisons of small optical depths. Optical thicknesses as large as 30 were observed. The trends seen in each plot continue for $\tau > 10$. Since the cloud heights depend on τ for thin clouds, it is not surprising that the results in Fig. 10 are similar to those in Fig. 9. The AVHRR ID optical depths are generally larger than the GOES values over the entire range of τ. The scatter about the line of agreement appears remarkably well balanced for all of the ice crystal models. Table 4 summarizes the results of all of the comparisons including $\Delta\tau$ in percent. Mean

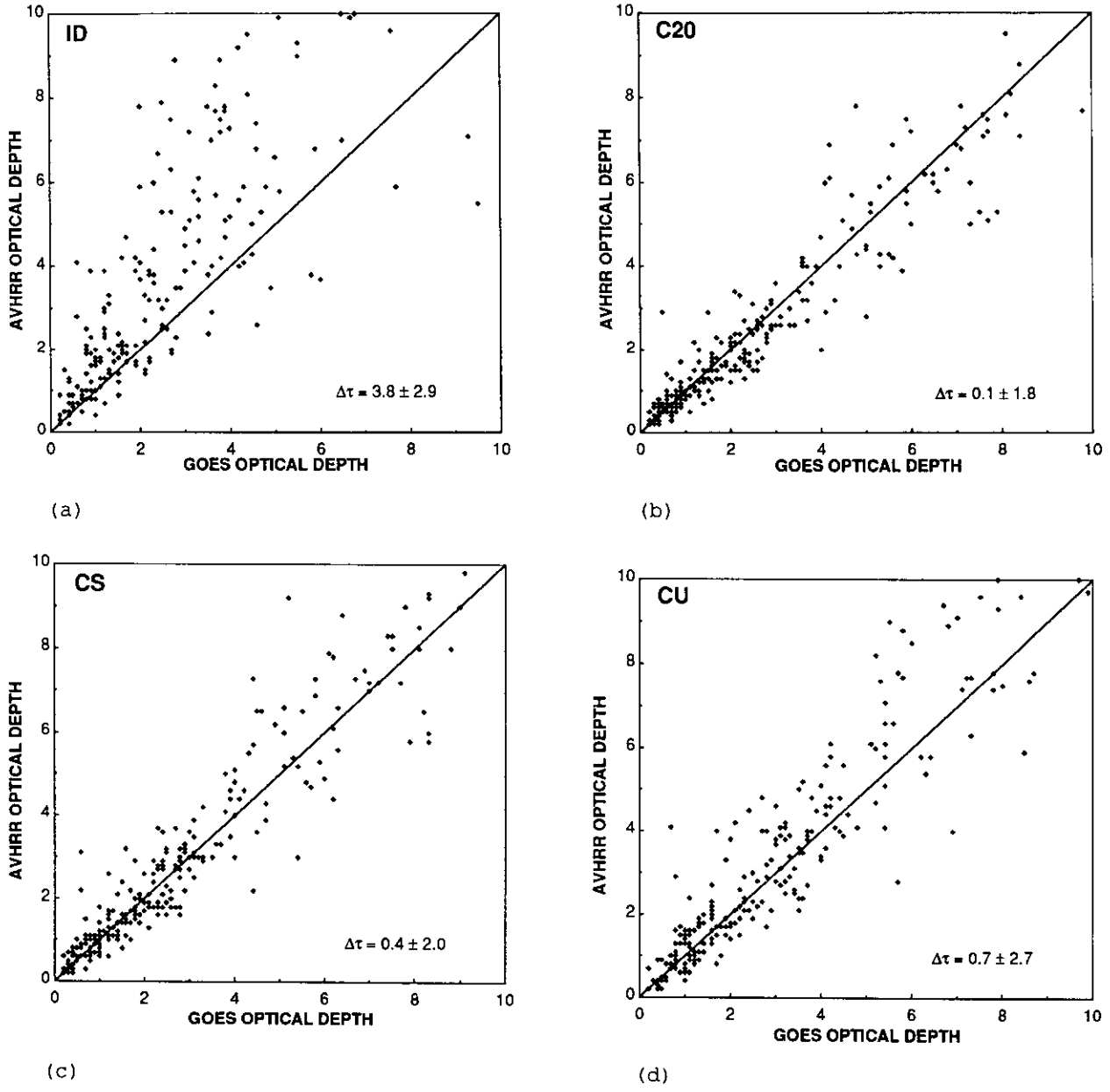

FIG. 10. Comparison of GOES and AVHRR optical depths for (a) ID model, (b) C20 model, (c) CS model, and (d) CU model.

values of τ and z_c derived from GOES are also given in the table.

The AVHRR ID optical depths are 67% greater than the GOES values, which results in the large cloud–altitude differences. A cursory examination of these results would suggest that the cloud height bias found with the ID model in the previous section should be almost twice the 1.3 km in Table 3. It should be realized, however, that most of the data were taken near 2030 UTC when the GOES position produced scattering angles near the cloudbow peak in the ID phase function (MLT). The GOES ID mean cloud height in Table 4 is only 0.4 km lower than the same data interpreted with the CS model. This small difference in the derived GOES cloud heights is exactly the same as that found by averaging the relative differences for the appropriate hours in Fig. 7 weighted by the number of observations. Therefore, the overall ID cloud-height error is probably not a simple sum of the errors in Tables 3 and 4. Considering all of the relative biases from the tables and from the ISCCP algorithm, however, it is reasonable to conclude that thin ($\tau < 6$) cirrus clouds interpreted with the ISCCP algorithm may be located approximately 1.5 to 2 km too low, on average over all scattering angles.

The optical depth differences were computed for each day to determine if there is any dependency of the agreement on the scattering angle pairs. The percentage differences are shown in Fig. 11 for each day. The symbols are spread horizontally on each day to provide separation. It is evident that on a given day corresponding to a particular set of scattering angles (Table 1), the optical depths computed using the ice-crystal models for the two satellites differ by less than 20%. During most days, the CS and C20 models show mean differences smaller than 10%. The ID optical depths, however, differ by more than 30% except on 27 October when there is virtual agreement in the optical depths for both the CU and ID models. The ratios of the phase functions for those two models are essentially the same (~ 1) for the scattering angles seen that day (Table 1). Thus, if one model shows agreement, the other should also. The ratios for the other two models are slightly less than unity. Only 15 data points were available for 27 October since the cirrus clouds were confined to a few regions in the northwestern corner of the grid (MHH). An average of 68 data points

TABLE 4. AVHRR–GOES comparison summary. All values referenced to GOES-derived quantities.

Model	z_c	Δz_c (km)	$\sigma(\Delta z)$ (km)	τ	$\Delta\tau$ (%)	$\sigma(\Delta\tau)$ (%)
ID	7.3	−1.2	1.3	5.6	67	52
C20	7.9	0.0	1.2	4.1	3	43
CS	7.7	−0.3	1.2	4.4	9	45
CU	7.0	−0.4	1.2	5.7	12	47

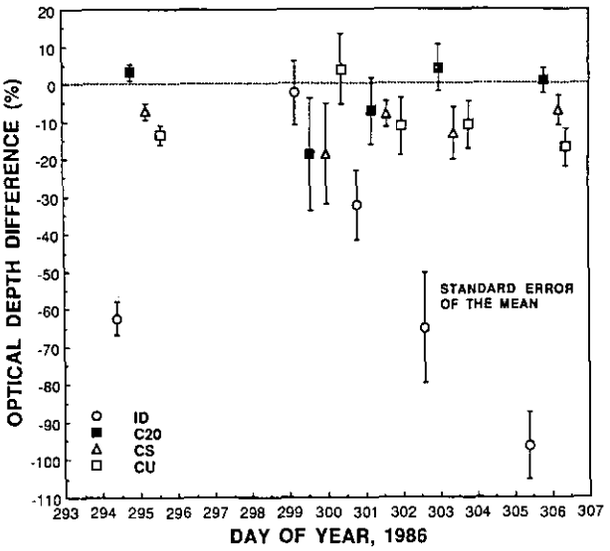

FIG. 11. Comparison of GOES–AVHRR, mean daily optical-depth differences over Wisconsin. Error bars indicate the standard error of the mean.

was available for the other 3 days. The good agreement of the CU optical depths may be happenstance or may be due to the occurrence of larger particles in those clouds than in the clouds observed during the other days. The former appears to be more likely. Despite the relatively good agreement in optical depth on 27 October, the CU and ID models underestimated the cloud heights by 2 km, while the CS and C20 models overestimated the cloud heights (as determined by the ER-2 for this area) by 0.1 km and 1.2 km, respectively.

The relatively small biases and comparable standard deviations for all three ice-crystal model results reflect the similarities in anisotropy typified in cloud bidirectional reflectance patterns presented by MLT. The slight differences in the theoretical reflectance patterns give rise to the observed biases. The good agreement found for both the CS and C20 optical depths is consistent with the lidar–satellite comparisons. Because of the small biases and relatively small variances, it is concluded that the reflectance patterns found in the theoretical CS and C20 models reasonably reproduce those observed in the cirrus clouds studied here. Due to the favorable height comparisons, it is also concluded that the optical depths derived with the C20 and CS models are sufficient to explain the IR and VIS radiances observed here.

5. Discussion

a. Error sources

The results shown above indicate that cirrus cloud height and optical depth can be determined to within ±1.3 km and 45%, respectively, using the CS or C20 model in the parameterization formulated earlier.

These uncertainties are considerably larger than those expected from the use of the parameterization instead of "exact" adding–doubling calculations. Based on Figs. 26 and 28 of MLT, rms uncertainties of only 33% in τ and $\sim$0.5 km in z_c are expected as a result of the parameterization for the conditions encountered in the observations. These values account for roughly 55% and 15% of the optical depth and height variances, respectively. Although difficult to quantify, there are numerous sources of error that may explain the remainder of the rms uncertainty in the derived properties.

The satellite-derived cloud height errors are based on comparisons with lidar data. The uncertainty in the lidar heights due just to the variation in the clouds around the site was estimated to be $\pm$0.7 km. Cloud center or effective cloud radiating altitude was determined graphically in most cases using plots containing some uncertainties due to the particular instrument characteristics. Assuming that the base and top heights are known to within $\pm$0.5 km on the plots, it is estimated that the physical center or radiative center was determined to the same precision. Thus, approximately 45% of the variance in the satellite- and lidar-derived cloud height differences may be attributed to the lidar analyses.

The AVHRR-GOES height-comparison standard deviations, however, are only slightly smaller than the lidar comparison values. Thus, most of the variance is probably the result of the interpretation of the satellite data. It was assumed in the modeling that the cirrus clouds are composed of regularly shaped, columnar ice crystals distributed in an infinite plane-parallel layer. From Figs. 1–4 and other examples (e.g., MYSAG and MHH), it is obvious that cirrus clouds infrequently occur in single, plane-parallel layers. They are often cellular, broken, multilayered, variably thick, and oriented in particular directions. Furthermore, while cirrus clouds often contain regular hexagonal ice columns, they commonly contain a variety of shapes such as flat plates, hollow columns, or aggregates (e.g., Heymsfield et al. 1990). The crystals may also be oriented so that their long axes are perpendicular to the fall direction (e.g., Thomas et al. 1990). At some temperatures, the clouds may be mixed phase so that they have radiative properties of both droplets and crystals. These features of real clouds are likely to induce significant variations in the radiative properties from one cirrus cloud to the next. The clouds observed in this study varied substantially in appearance from one day or area to the next. Interpretation of these variable radiative properties with a single model will undoubtedly cause significant errors in the retrieved optical depth or cloud altitude.

For thin clouds, errors in the clear-sky reflectance are important. These arise from variations in soil moisture and aerosol loading and from uncertainties in the clear-sky anisotropic reflectance model. Uncertainties in the clear-sky temperature can also affect the derived cloud height. Values for T_s are usually taken from surrounding clear areas or times and, therefore, may not be exactly the temperature underlying the cloud. Atmospheric soundings, especially those from satellites, contain some inherent uncertainties that will cause some misplacement of the derived cloud temperature in height coordinates. Interpolation and extrapolation of soundings to other times and locales will induce some additional uncertainty in the sounding for the time and place of the analyzed satellite data. Satellite calibration inaccuracies will also affect the placement of the cloud and the determination of the optical depth. Intercomparison of the AVHRR and GOES reflectances and temperatures taken during the 28 October *NOAA-9* overpass revealed that the two satellites are intercalibrated with a precision better than 1% for both the IR and VIS channels. Slight misnavigation of the images will introduce scatter into the results. Small time differences in the images of only a few minutes are sufficient to introduce significant variance for regions less than 50 km wide.

All of these error sources together are sufficient to explain the observed variance in the observation intercomparisons. It may be inferred from the sizes of the uncertainties (Tables 3 and 4) that the parameterization errors are the same magnitude or smaller than the other errors in the analysis process. Thus, it is concluded that additional accuracy in the reflectance and emittance parameterizations (MLT) is unnecessary at this time. Simpler parameterizations such as those of Platt et al. (1980) and MYSAG would produce larger variances and, perhaps, significant biases in the optical depths (MLT). Given the complexities of clouds and the potential error sources discussed above, it is encouraging that the VIS–IR parameterization using the simple hexagonal ice-crystal models produced the level of cloud height precision observed in the comparisons.

b. Cloud heights

The comparisons have been used to show that the cirrus cloud heights derived over backgrounds of nominal albedo are underestimated by an average of $\sim$1.5 km using the ISCCP algorithm. It has also been demonstrated that using the current algorithm for these same clouds, the CS and C20 models yield mean cloud heights that are within $\pm$0.3 km of the lidar estimates of the cloud center. The CU model, however, yielded a mean underestimate of $\sim$1.3 km. Based on the sample variances and the Student's t-test, it is concluded that the mean cloud height differences between the various models and the lidar data are significant at a confidence level greater than 99%.

Since the mean clear-sky albedos of water and most vegetated land are similar to those observed here, it

follows that the ISCCP algorithm and ID-model biases will affect the cirrus cloud heights derived over most of the globe. The level of error exceeds the ±1 km prescribed for the ISCCP (Schiffer and Rossow 1983). Raising the mean cloud heights of cold clouds having $\tau < 6$, say, by 1.5 km is one means to account for the model errors. This solution would probably eliminate the mean bias but would introduce other problems. For example, the consistency between the derived values and measured radiances would be destroyed. Furthermore, other biases due to the nature of the scattering patterns would remain. A majority of the ISCCP data come from geostationary satellites so that the viewing angles for a given region are fixed at any particular time of day and season. Part of the height bias results from differences in the scattering patterns, not just from the asymmetry parameter. Since the scattering angles are constant when the viewing and illumination angles are fixed, the relative bias between the ID and the CS models, for example, will be dependent on the time of day as seen in Fig. 7. Therefore, apparent diurnal variations in cirrus cloud heights may be induced by analyzing the data with the wrong microphysical model. Such problems will not be eliminated by simply adjusting the mean cloud height.

It is desirable to analyze the radiance data with the most realistic model available. The CS model produced the smallest bias error in the lidar comparisons, while the C20 model provided the greatest degree of consistency in the dual-satellite comparisons. The magnitudes of the errors in both cases are about equal, indicating that of the four tested either the CS or C20 model is the most realistic for interpreting the cirrus clouds observed in this study.

c. *Optical depths*

Aside from the cloud height errors, there are significant optical depth differences that must be considered. One of the primary uses of global cloud climatologies is climate model validation. For example, a cloud parameterization scheme used in a climate model may compute a certain amount of liquid water or ice water in a given grid box. In addition to latent heat release, this condensation or freezing changes the grid-box optical properties that alter the radiative energy exchange in the box. These energy transformations are critical to subsequent changes in the circulation through the grid box and its neighbors.

One means of determining if the model development is realistic is to compare certain bulk parameters computed by the model with long-term averages of observations of the same variables. Satellite-derived optical depths, albedos, cloud fractions, and longwave fluxes are all variables used for these purposes (e.g., Slingo et al. 1987; Potter et al. 1988). To achieve the highest degree of realism, the cloud parameterization must be able to condense or freeze the proper amount of water into the microphysical distribution necessary to produce the average observed radiative conditions. The amount of liquid or ice water needed to produce the observed conditions depends on the microphysical distribution assumed for the cloud. The amount of latent heat release depends on the amount of water vapor that changes state. Thus, the microphysics of the cloud are a critical link between the radiative and latent energy transformations in a cloud.

One measure of liquid or ice water content is the variable, liquid (ice) water path or LWP. This quantity is related to the optical depth. In simple terms,

$$\mathrm{LWP} = \rho_L N_0 V \Delta z$$

and

$$\tau = Q_{ex} N_0 A \Delta z,$$

where ρ_L is the density of liquid or ice water, Δz is some arbitrary distance, N_0 is the effective number density of the particles, Q_{ex} is the extinction efficiency, and V and A are the effective volume and cross section of the particles in the distribution. For a given distribution,

$$\mathrm{LWP} = \frac{\rho_L V \tau}{Q_{ex} A} \tag{7}$$

in grams per square meter. For the sizes of particles considered here, $Q_{ex} \approx 2$. Thus, the inference of an optical depth implies a measurement of liquid or ice water.

For example, Eq (7) yields LWPs of 6.0τ and 6.7τ in g m^{-2} for the C20 crystal and 10-μm water droplet, respectively. Considering the clouds observed here, the mean optical depth derived using the ID model (Table 3) is 1.7 times greater than the C20 result. Thus, a cloud parameterization that employs an ID microphysical model would have to condense and freeze almost twice the amount of water to match the cirrus observations of radiance or τ than it would using a C20 model. This extra mass of changed phase would dramatically increase the latent heat release and alter the grid-box energy balance. The generated albedo would match the observations but the hydrological and thermodynamical components would be incorrect, leading to errors downstream in the model calculations.

The actual differences in LWP between the droplet and crystal models for a given τ vary considerably from one model to the next because of the geometry of the ice crystals. It is clear from the above illustration, however, that consistency between the cloud microphysics and optical properties is essential for proper utilization of the observations and the generation of clouds in the

models. This study has shown that the radiance fields from the cirrus clouds are most consistent with those produced theoretically by the CS and C20 models. These same models also produce the best agreement between lidar and satellite measurements of cloud height. Consistency between the microphysics and LWP has not been shown, however. The optical depths derived using the two models are not much different. The size distribution and effective radii of the models are significantly different. Thus, the LWP inferred from a given optical depth for the C20 will be not be the same as that from the CS. This discrepancy has not been resolved. Perhaps future datasets from Phase II of FIRE will provide sufficient in situ microphysical data to begin resolution of this issue. Nevertheless, it may be concluded at this point that the ID model significantly overestimates the optical depths of cirrus (ice) clouds. A much better estimate can be obtained with use of the CS or C20 model.

d. Analysis application

The methodology and parameterizations developed here have been tested in the most ideal conditions to better understand the results. Clouds occur in multiple layers or, in the case of convective clouds, nondiscrete layers, which confuse the interpretation. Thus, the level of accuracy found for the current study may not always be realized in multiple cloud-layer conditions. Furthermore, the comparisons with observations have been taken over midlatitude cirrus clouds and backgrounds having $\alpha_{sd} < 0.16$ and have included only a few of the possible viewing and illumination conditions. The results of this study indicate that the models perform well at various angular configurations, so that any significant increases in errors due to view angles are not likely. Other cirrus clouds such as those in the tropics, however, may be at much higher altitudes with the potential for greater thermal contrast and different microphysics. The possible effects of these differences are unknown and require further examination. It is expected that the accuracy of inferred cloud optical depth decreases as the background albedo increases. Thus, larger errors in τ and z_c are likely for VIS–IR retrievals over deserts, ice, snow, and other clouds. Study of these errors will be possible as lidar measurements over these surfaces become available.

Application of the methodology in an operational mode will require some alterations. Current algorithms simply treat each pixel or a group of pixels as belonging to a certain layer. The ISCCP algorithm operates with a seven-layer atmosphere compared to the three layers used here. The current methodology can be easily adapted to a more highly resolved vertical structure. Because of potential layer overlap in the small-optical-depth portions of the histograms, some additional decision trees must be developed to accommodate the averaging processes employed here. Simply providing more layers in the analysis, however, does not necessarily provide better height resolution of the data. There is the potential for considerable scatter in the data, which could result in the placement of individual pixels in the wrong layer. Thus, the issue of including more layers needs further study.

In future applications of the methodology, either the CS or C20 model would be used for cloud layers where $T < 253$ K. Without additional information about phase, either a mixed-phase or water-droplet model would be employed for layer temperatures between 253 K and 273 K because of the common occurrence of supercooled water droplets. A water-droplet model would be employed for all layers having $T > 273$ K. Most of the cloud temperatures in this study were for $T < 253$ K, so there is limited information available for selecting the optimum phase function for the mid-range of cloud temperatures.

6. Concluding remarks

A methodology was developed to analyze satellite data using a variable-microphysics parameterization of VIS reflectance and IR emittance. It was then applied to GOES satellite data coincident with lidar measurements of cloud height. A comparison of the results to the lidar data showed that, on average, the ID model representing the current ISCCP model produces a 1.3-km underestimate of the cloud height, while the mean CS and C20 ice-crystal model results are within ±0.3 km of the lidar values. The large-particle CU model yielded the same cloud height errors found for the ID model. An additional underestimate of 0.3 km is expected when the ISCCP technique of analyzing each pixel is used instead of preliminary averaging of certain portions of the data. The standard deviation about the mean difference for the comparisons is 1.3 km.

Intercomparison of cirrus cloud heights and optical depths using dual-satellite measurements produced comparable statistics for the cloud heights derived with the CS and C20 models. The CS and C20 optical depths derived from the GOES data were reproduced to within ±45% using the AVHRR data from different angles. The bias errors are 9% and 2%, respectively. The CU model also produced reasonable agreement between the GOES- and AVHRR-derived optical depths. The ID model produced optical depth bias errors of 67%.

It is concluded that the CS and C20 models are superior to the ID and CU models for interpreting the radiance fields over cirrus clouds. The optical depths derived with the CS and C20 models adequately account for the cloud emittances, while the reflectance patterns produced by these models are very consistent with the observations. The reflectance patterns pro-

duced by the ID model did not agree well with the observations. The ID optical depths were also too high to account for cloud emittance. From the combined lidar and dual-satellite analysis, it is concluded that use of the ISCCP algorithm to interpret radiances from thin cirrus clouds results in cloud height underestimates of 1.3 to 1.6 km and optical depth overestimates of up to 70%.

Real cirrus clouds are typically composed of complex particles having various shapes and sizes. A cloud containing only randomly oriented, perfectly shaped, hexagonal columns probably does not exist. Furthermore, optical phenomena (e.g., halos) associated with cirrus clouds are seen less often than not. This suggests that the idealized phase functions used here, which reproduce such phenomena, should not account for the reflectance characteristics of the majority of cirrus clouds. The evidence presented here, however, is a very strong indication that the phase functions of real cirrus particles are very similar to the CS and C20 phase functions, at least over the range of scattering angles examined in this paper ($75° < \Theta < 180°$). Although they are idealizations, these phase functions represent a dramatic improvement in the representation of scattering from cirrus clouds over simple Mie scattering. It is also clear that phase functions of ice cylinders are no better than Mie spheres for modeling cirrus scattering. The cylindrical phase functions (e.g., Liou 1973) are similar to the ice crystal phase functions in that they have greater values than equivalent Mie spheres at side-scattering angles ($\Theta \approx 90°$). The cylinder scattering, however, has a rainbow peak corresponding to the water droplet rainbow and is much less than that of spheres for $\Theta > 160°$, the opposite of the ice-crystal phase function. The results presented here for the ice-crystal models were consistent over the observed range of Θ. Thus, the optical depths for those cases having $\Theta > 160°$ would have been overestimated much more with the cylindrical phase function than they were with the ID model.

Limited ranges of angles, surface albedos, and clouds were used in this study. Greater rms differences are expected over brighter surfaces while smaller differences should be realized over darker surfaces such as water. The study should be expanded to intercompare similar datasets taken in different circumstances. Further examination of the radiance fields, lidar data, and collocated in situ microphysical data will undoubtedly reveal new aspects of cirrus clouds and perhaps shed new light on the relationships between microphysical properties, ice water content, and optical properties. Additional study of the phase functions for small, hollow, and aggregate crystals and for mixed phase conditions should be continued since they are commonly seen in the in situ measurements.

A repeat of the analyses performed in this study using different sets of angles, surfaces, and cloud heights, however, will probably have little effect on the basic conclusions: a radiative transfer model using a spherical water-droplet phase function to interpret radiances from cirrus clouds will produce biased results. Cirrus clouds are primarily composed, not of water or ice spheres, but of ice crystals built on a molecular-scale, hexagonal column framework. The parameterizations in Part I (MLT) and the results presented here provide the bases for much improved interpretation of satellite measurements of cirrus clouds.

Acknowledgments. This work represents part of the Ph.D. dissertation of Patrick Minnis. Special thanks to K. Sassen of the University of Utah, J. M. Alvarez of NASA Langley Research Center, J. D. Spinhirne of NASA Goddard Space Flight Center, and C. J. Grund of NOAA/ERL for providing their lidar data. D. R. Doelling and B. J. Byars of Lockheed Engineering and Sciences Company assisted in the reduction of the satellite data.

REFERENCES

Heymsfield, A. J., K. M. Miller, and J. D. Spinhirne, 1990: The 27–28 October 1986 FIRE IFO Case Study: Cloud measurements. *Mon. Wea. Rev.*, **118,** 2313–2328.

Liou, K. N., 1973: Transfer of solar irradiance through cirrus cloud layers. *J. Geophys. Res.*, **78,** 1409–1418.

Minnis, P., and E. F. Harrison, 1984: Diurnal variability of regional cloud and clear-sky radiative parameters derived from GOES data, Part I–III. *J. Climate Appl. Meteor.*, **23,** 993–1052.

——, ——, and G. G. Gibson, 1987: Cloud cover over the eastern equatorial Pacific derived from July 1983 ISCCP data using a hybrid bispectral threshold method. *J. Geophys. Res.*, **92,** 4051–4073.

——, P. W. Heck, and E. F. Harrison, 1990a: The 27–28 October 1986 FIRE IFO Cirrus Case Study: Cloud parameter fields derived from satellite and lidar data. *Mon. Wea. Rev.*, **118,** 2426–2446.

——, D. F. Young, K. Sassen, J. M. Alvarez, and C. J. Grund, 1990b: The 27–28 October 1986 FIRE IFO Cirrus Case Study: Cirrus parameter relationships derived from satellite and lidar data. *Mon. Wea. Rev.*, **118,** 2402–2425.

——, K.-N. Liou, and Y. Takano, 1993: Inference of cirrus cloud properties using satellite-observed visible and infrared radiances. Part I: Parameterization of radiance fields. *J. Atmos. Sci.*, **50,** 1279–1304.

Platt, C. M. R., and A. C. Dilley, 1984: Determination of the cirrus single-scattering phase function from lidar and solar radiometric data. *Appl. Opt.*, **23,** 380–386.

——, D. W. Reynolds, and N. L. Abshire, 1980: Satellite and lidar observations of the albedo, emittance and optical depth of cirrus compared to model calculations. *Mon. Wea. Rev.*, **108,** 195–204.

Potter, G. L., R. D. Cess, P. Minnis, E. F. Harrison, and V. Ramanathan, 1988: Diurnal variability of the planetary albedo: An appraisal with satellite measurements and general circulation models. *J. Climate,* **1,** 233–239.

Rossow, W. B., L. C. Garder, P. Lu, and A. Walker, 1988: International Satellite Cloud Climatology Project (ISCCP), Documentation of cloud data. WCRP Rep. WMO/TD-No. 266, 122 pp. [Available from Dr. W. B. Rossow at NASA Goddard Space Flight Center, Institute for Space Studies, 2880 Broadway, New York, NY, 10025.]

Sassen, K., and K.-N. Liou, 1979: Scattering of polarized laser light by water droplet, mixed-phase, and ice crystal clouds. Part I: Angular scattering patterns. *J. Atmos. Sci.*, **36,** 838–851.

——, C. J. Grund, J. Spinhirne, M. Hardesty, and J. M. Alvarez, 1990: The 27–28 October 1986 FIRE cirrus case study: A five-lidar view of cirrus cloud structure and evaluation. *Mon. Wea. Rev.*, **118,** 2288–2311.

Schiffer, R. A., and W. B. Rossow, 1983: The International Satellite Cloud Climatology Project (ISCCP): The first project of the World Climate Research Programme. *Bull. Amer. Meteor. Soc.*, **64,** 779–784.

Slingo, A., R. C. Wilderspin, and S. J. Brenthall, 1987: Simulation of the diurnal cycle of outgoing longwave radiation with an atmospheric GCM. *Mon. Wea. Rev.*, **115,** 1451–1457.

Spinhirne, J. D., D. L. Hlavka, and W. D. Hart, 1988: ER-2 lidar observations from the October 1986 FIRE cirrus experiment. NASA TM 100704, 49 pp. [NTIS-N89-21444.]

Starr, D. O'C., 1987: A cirrus-cloud experiment: Intensive Field Observations planned for FIRE. *Bull. Amer. Meteor. Soc.*, **68,** 119–124.

Takano, Y., and K. N. Liou, 1989: Radiative transfer in cirrus clouds: I. Single-scattering and optical properties of oriented hexagonal ice crystals. *J. Atmos. Sci.*, **46,** 3–20.

Thomas, L., J. C. Cartwright, and D. P. Wareing, 1990: Lidar observations of the horizontal orientation of ice crystals in cirrus clouds. *Tellus,* **42B,** 211–216.

Wielicki, B. A., J. T. Suttles, A. J. Heymsfield, R. M. Welch, J. D. Spinhirne, M.-L. C. Wu, D. O'C. Starr, L. Parker, and R. F. Arduini, 1990: The 27–28 October 1986 FIRE IFO Cirrus Case Study: Comparison of radiative transfer theory with observations by satellite and aircraft. *Mon. Wea. Rev.*, **118,** 2356–2376.